FISEVIER

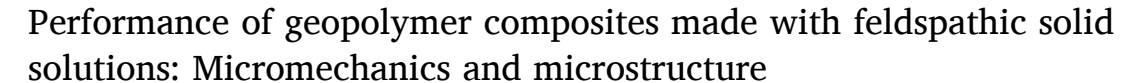
Contents lists available at ScienceDirect

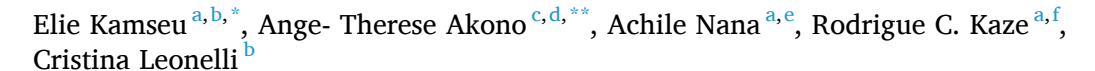
Cement and Concrete Composites

journal homepage: www.elsevier.com/locate/cemconcomp



Research Paper





- ^a Laboratory of Materials, Local Materials Promotion Authority, MINRESI/MIPROMALO, P.O. Box 2396, Yaoundé, Cameroon
- ^b Department of Engineering "Enzo Ferrari", University of Modena and Reggio Emilia, Via P. Vivarelli 10, 41125, Modena, Italy
- ^c Department of Civil and Environmental Engineering, Northwestern University, Evanston, IL, 60208, USA
- ^d Department of Mechanical Engineering, Northwestern University, Evanston, IL, 60208, USA
- ^e Research Unit of Noxious Chemistry and Environmental Engineering, Faculty of Science, Department of Chemistry, University of Dschang, P.O. Box 67, Dschang, Cameroon
- f Laboratory of Applied Inorganic Chemistry, Faculty of Science Department of Inorganic Chemistry, University of Yaoundé I, P.O. Box 812, Yaoundé, Cameroon

ARTICLE INFO

Keywords: Inorganic polymer cements Nanoindentation Hardness Scratch tests Young's modulus High-performance composites

ABSTRACT

This study investigates the high performance of feldspathic solid solution-based geopolymer composites. The results show that a feldspathic solid solution with incongruent dissolution in an alkaline medium produces a differential amount of N-A-S-H+ polysialate geopolymer, depending on the mineral nature of the raw solid precursor. In turn, the presence of both N-A-S-H and polysialate geopolymer reduced the cumulative pore volume to a nanometric size, leading to flexural and compressive strengths in the range of 26–36 MPa and 86–100 MPa, respectively. The limited dissolution in the alkaline medium of the feldspathic powders allowed for a direct correlation among the Young modulus, the hardness, and the N-A-S-H + polysialate geopolymer. The findings show that when the amount of N-A-S-H and polysialate geopolymer is sufficient to cover the incongruent dissolved grains of solid solutions with no excess of geopolymer gel, the bonding strength developed exhibits high mechanical performance in the final composite The results confirm the possibility of reproducing dimensioned stones by geopolymerizing the feldspathic solid solutions.

1. Introduction

Inorganic polymer cements (IPCs), also referred to as geopolymers, consist of tetrahedral AlO_4 and SiO_4 units polycondensed into three-dimensional structures. IPCs are the products of the reaction between aluminosilicate minerals and highly concentrated alkaline solutions [1, 2]. IPCs present a low embodied energy alternative to conventional ordinary Portland cement (OPC) composites. Unlike OPC composites, IPCs release less carbon dioxide emissions during their synthesis [3–5]. Moreover, IPCs have shown excellent properties such as high mechanical strength, thermal stability, and resistance to chemical attack [6–8]. They have also demonstrated a strong potential for application in thermal insulators, refractories, and coatings [9–12].

Currently, metakaolin (MK) is the most common aluminosilicate source and the standard solid precursor for IPCs due to its purity and high reactivity in an alkaline medium. However, MK requires energy-intensive thermal treatment to develop amorphous phases. MK results from the thermal activation of kaolinite clay minerals, such as kaolin and halloysite. This thermal activation occurs at temperatures of $500-850\,^{\circ}$ C, and the duration depends on the clay mineral crystallinity [13,14]. After thermal activation, amorphous phases with high pozzolanic properties, such as Al_2O_3 and SiO_2 , are formed [15]. In addition to the need for high-energy thermal treatment, other limitations of MK-based IPCs include the increased water demand to achieve good workability as well as their high porosity, which negatively affects their mechanical strength and long-term durability [13].

Recent studies have investigated alternative aluminosilicate sources to overcome the limitations of MK. For instance, some studies have introduced low fractions of semi-crystalline compounds, such as basalt, pegmatite, and nepheline syenite, thereby enhancing the

^{*} Corresponding author. Laboratory of Materials, Local Materials Promotion Authority, MINRESI/MIPROMALO, P.O. Box 2396, Yaoundé, Cameroon.

^{**} Corresponding author. Department of Mechanical Engineering, Northwestern University, Evanston, IL, 60208, USA. *E-mail addresses*: kamseuelie2001@yahoo.fr (E. Kamseu), ange-therese.akono@northwestern.edu (A.T. Akono).

microstructural and mechanical properties of IPCs. Overall, most of the focus has been on industrial by-products (e.g., coal fly ash and metallurgical slag), natural volcanic ash, biomass (e.g., rice husk ash), and laterites [11,14,16–19]. Yet, low-energy alternatives such as feldspar solid solutions have received far less attention.

Feldspars are natural rocks with a framework structure of Al-Si minerals [20]. They are mainly divided into the sub-groups plagio-clases (Na-CaAl $_2$ Si $_2$ Oa, Al $_2$ Si $_2$ Oa, alkali-feldspar albite (NaAlSi $_3$ Oa), and microcline (KAlSi $_3$ Oa) [21,22]. Compared with clay kaolinite (Al $_2$ Si $_2$ Oa) (OH) $_4$), the feldspar structural network does not contain crystallization water, and the water molecules trapped in cavities are quickly evaporated at low temperatures. As a result, feldspar solid solutions do not require thermal activation before their geopolymerization.

Few studies have been conducted to investigate the properties and performance of (feldspathic aluminosilicate) particle-based geopolymers. Feldspathic geopolymers exhibit high strength, a homogeneous and dense microstructure with very low porosity, and superior performance at high temperatures [4,13,23-26]. The higher performance of feldspathic geopolymers is due to the presence of new M₂O-Al₂O₃-SiO₂-H₂O (M-A-S-H) and CaO-Al₂O₃-H₂O (C-A-H) phases, which result from the reaction between aluminate and silicate groups present within the solid solution. Due to their size, the fine reactive powders promote the formation of binders within meso- and macropores. Moreover, hybrid particles/MK-based geopolymer composites exhibit better mechanical properties compared to MK-based geopolymers. Xu and van Deventer [20] attributed this mechanical enhancement to the higher Si/Al ratio in feldspathic powders; the Si/Al ratio increases with the M-feldspar/MK ratio, where M is K or Na. The properties improve when the fine particles play a double function as reactive particles to induce geopolymerization and as fillers for structural reinforcement. As reactive particles, the fine particles undergo a partial dissolution: Al and Si species dissolve and start polymerizing AlO₄ and SiO₄ groups into a three-dimensional structure, leading to the formation of geopolymer gel at the particles' surface. The unreacted portions of these fine particles act as reinforcement of the geopolymeric

In this work, we investigated IPCs synthesized using fine feldspar solid solutions powders. This study built upon our prior investigation [26] in which we introduced a preliminary model for a feldspar solid solution geopolymer. However, the influence of the amorphous/crystalline ratio of the reactive phases on the partial dissolution of particles and on the properties of geopolymer composites is still unclear. In this study, three solid solutions based on aluminosilicate sources granite, pegmatite, and quartz—were selected to design particle-based IPCs. The fine particles were altered by 15-25 wt% of calcined clay. Calcined clays —MK and meta-halloysite (MH)— were added to increase the fraction of amorphous phases, hence enhancing the reactivity of the solid precursors. Therefore, we extend our feldspar-geopolymer model to include other calcined clays, such as MH. Moreover, we applied multiscale mechanical testing, analytical methods, micromechanical methods, and fracture analysis to provide a basic understanding of the performance and pore structure of feldspar-based IPCs.

2. Materials and methods

2.1. Materials

For the preparation of feldspathic solid solution-based geopolymer composites, granite and pegmatite were collected from Dschang (West Province of Cameroon) and Kribi (South Province, Cameroon), respectively. Quartz sand from Yaoundé (Central Province) was used for comparison. These materials were used as the main solid precursors for the design of the geopolymer. To improve the reactivity of the solid precursors, MH or MK was incorporated in small proportions. Both calcined clays were obtained by calcining halloysite from Balengou

(West Province) and kaolin from Bafut (Northwest Province) at 700 °C for 4 h. All the raw materials from Cameroon used in this study have been previously used in other investigations [13,14,26], which can be consulted for more details. The raw materials were finely ground with a grinder for 6 h (1200 rpm) to a median size of 63 μm . The chemical composition of the solid precursors was determined using x-ray fluorescence analysis (see Table 1). Pegmatite, MK, and MH contained SiO₂ and Al₂O₃ as major oxides, whereas the quartz sand was mainly composed of just SiO₂.

A 10-M NaOH aqueous solution was prepared by diluting a commercial pellet of NaOH with 99% purity. A commercial sodium silicate solution (26.45 wt% SiO_2 and 9.11 wt% Na_2O , SiO_2/Na_2O ratio = 3.0, density = 1.38 g/cm³) and sodium hydroxide solution were used to prepare the hardener. Both commercial solutions were provided by Ingessil s.r.l. (Verona, Italy).

2.2. Preparation of geopolymer composites

During the preparation of the geopolymer composites, the solid solutions (pegmatite, and granite), and quartz sand were altered with 15–25 wt% MH or MK and activated with an alkaline solution (prepared by mixing sodium hydroxide and a silicate solution at a ratio of 1:1). Table 2 summarizes the formulations considered in this study: Q, P, R1, R2, R3, and D. The activator solution/solid precursor ratio was kept constant at 0.38, with suitable workability of pastes. Immediately after mixing, the fresh pastes were cast into different molds. Before demolding, the samples were hardened in plastic bags for 72 h. The hardened composites were cured for 28 days (laboratory conditions: $22\pm3\,^{\circ}\text{C}$, $54\%\,$ humidity) prior to characterization.

2.3. Grinding and polishing procedure

A grinding and polishing procedure was employed to prepare the specimen surface before nanoscale characterization (scratch testing or grid nanoindentation testing). The grinding and polishing procedure consists of three steps: cold mounting using a low-viscosity epoxy resin, precision sectioning using a low-speed diamond saw, and grinding and polishing using a semi-automated grinder polisher. Grinding was performed using silicon carbide polishing pads ranging in fineness from 50 μm to 10 μm . Polishing was conducted using plain-woven polishing pads along with polycrystalline diamond slurries with particle sizes of 3 μm , 1 μm , and 0.25 μm . In between each step, the specimens were cleaned in an inert solvent using ultrasonic waves to prevent cross-contamination. Afterward, the polished specimens were stored in vacuum desiccators.

2.4. Characterization of geopolymer composites

2.4.1. Flexural strength tests

Three-point flexural strength tests were conducted using specimens with a nominal size of 10 ± 0.10 mm width, 10 ± 0.10 mm thickness, and 100 ± 0.10 mm length. Five tests were conducted for each formulation. Each flexural strength test was conducted as follows. First, the geopolymer composites was placed in an indicated sample holder. Then, the sample was loaded in a testing machine (type 810, MTS, USA) with a crosshead speed of 3 mm \times min $^{-1}$. The span between the two platens of the sample holder was 40 mm. Meanwhile, the loading piston and supports were steel knife edges rounded to a radius of 1 mm. The load was applied at the mid-point of the test sample. The flexural strength was computed according to Eq. (1):

$$\sigma = \frac{3Fl}{2bh^2} \tag{1}$$

where σ is the maximum canter tensile stress (in MPa); F is the maximum load at fracture (in N); and l, b, and h are the distance between the supports, the width, and the thickness of the specimens, respectively (in

 Table 1

 Chemical composition of solid precursors (wt.%).

wt.%	SiO_2	Al_2O_3	Fe ₂ O ₃	CaO	MgO	Na ₂ O	K ₂ O	TiO ₂	L.O.I
Metakaolin	70.25	28.03	0.75	0.10	0.08	0.05	0.07	0.66	/
Metahalloysite	56.00	29.30	2,60	/	/	/	0.01	0.30	
Granite	76.13	13.44	0.20	0.34	0.86	4.21	3.46	1.44	1.31
Sand	96.94	0.90	0.35	0.37	0.15	0.38	0.29	0.49	1.12
Pegmatite	73.39	15.13	0.33	0.24	0.05	4.51	5.09	0.01	0.47

Table 2
Composition of different formulations (wt.%).

Formulations notation	Granite	Quartz	Pegmatite	MK	MH
Q	-	80	_	-	20
P	85	_	_	-	15
R1	-	_	75	-	25
R2	-	_	80	-	20
R3	-	_	85	-	15
D	-	-	85	15	-

mm).

2.4.2. Compression strength tests

Compression tests were carried out to investigate the strength of samples after 28 days of curing. The tests were performed with an automatic hydraulic press (Impact Test Equipment Ltd., Stevenston, Scotland). The hydraulic press had a capacity of 250 kN, and the loading rate was set at 0.500 MPa/s according to the EN196/01 standard. Cubic specimens of 50 ± 0.10 mm were subjected to a compressive load at an average rate of 3 mm \times min $^{-1}$ until failure. For each formulation, at least five samples were tested to determine the average value of the compressive strength.

2.4.3. Fracture toughness tests

The fracture toughness was evaluated using microscopic scratch testing. A sphero-conical probe was pushed across the surface of polished specimens under a linearly increasing prescribed vertical force. The prescribed maximum vertical force was 5.5 N, the scratch length was 3 mm, and the scratching speed was 6 mm/min. The resolution on the force measurements was 0.1 mN, and the resolution on the penetration depth was 0.3 nm. For each formulation, 11 tests were conducted. To compute the fracture toughness K_c , a nonlinear fracture mechanics model was applied based on previous studies [27–29]:

$$\frac{F_T}{\sqrt{2pA}} = K_c \mathcal{F}(\frac{d}{R}) \tag{2}$$

where F_T is the measured horizontal force, d is the penetration depth, and R is the scratch probe tip radius. The probe shape function 2pA was calibrated based on Akono and Ulm procedure [30]. Post-testing, environmental scanning electron microscopy was utilized to observe the fracture micro-mechanisms. To this end, an FEI Quanta 650 environmental scanning electron microscope (ESEM; FEI) was used on the low vacuum mode.

2.4.4. Grid nanoindentation tests

To assess the microstructural origin of the strength and stiffness of the geopolymer composite specimens, grid nanoindentation was employed in concert with statistical deconvolution. Grid nanoindentation consists of conducting an array of nanoindentation tests: a 21×21 pattern was employed with an inter-indent grid spacing of 25 μ m. Each nanoindentation was characterized by a maximum vertical force of 2 N, a loading/unloading phase of 30 s, and a holding phase of 5 s. The resolution on the vertical force was 20 nN and the resolution on the penetration depth was 0.01 nm. For each nanoindentation test, the indentation modulus M and indentation hardness H were computed

using the Oliver and Pharr method [31,32]:

$$M = \frac{\sqrt{\pi}}{2} \frac{S}{\sqrt{A(h)}}; H = \frac{P_{max}}{A(h)}$$
 (3)

where h is the penetration depth, P is the vertical force, S is the unloading slope of the P-h curve, and A is the projected contact area. Before testing, the projected contact area function was calibrated using fused silica as a reference material [31]. To assess the microconstituents, we performed a statistical deconvolution analysis. According to the principle of statistical deconvolution, to represent the distribution of the indentation moduli and indentation hardness values as a mixture of individual phases, each phase of each material must be characterized by a Gaussian distribution [33,34]. We utilized an expectation maximization algorithm along with a Bayesian information criterion to identify the optimum number of phases [35].

2.4.5. Scanning electron microscopy and X-Ray diffraction analyses

The microstructure of the geopolymer composite specimens was investigated using an ESEM (Quanta 200, FEI 650) on the low vacuum mode. The advantage of this technique is that the relative humidity can be controlled by both the water vapor pressure and the temperature in the ESEM chamber. Polished specimens from the flexural testing were used for microstructural investigations. In particular, the ESEM can avoid the influence of cracks and facilitate the investigation of phase distribution in the matrices.

Moreover, mineralogical composition analyses of the raw materials and geopolymer composites were carried out with an X-ray powder diffractometer (XRD; PW3710, Phillips Healthcare) Cu K α , Ni-filtered radiation (at a wavelength of 1.54184 Å). The radiation was generated at 40 mA and 40 kV. Specimens were step-scanned as a random powder from 5° to 70° in the 2 θ range and then integrated at a rate of 2 s per step.

Infrared spectra were recorded on finely crushed powder of each consolidated formulation using an infrared Fourier spectrometer (Avatar 330 FTIR, Thermo Nicolet) in the range of $400-4000~{\rm cm}^{-1}$. For the analysis, each powdered sample was prepared by suspending it in a suitable solvent such as ${\rm CH_2Cl_2}$ in a small test tube and transferring onto a KBr plate. A second KBr plate was placed on top and a quarter turn was made to obtain a nice even film. The plates were placed into the sample holder and a spectrum ran through it. 32 scans for background and 32 scans per sample were made with signal gain of 1 and a resolution of 4 ${\rm cm}^{-1}$.

2.4.6. Mercury intrusion porosimetry

To evaluate the pore size distributions of all formulations, mercury intrusion porosimetry (MIP) was performed using an Autopore IV 9500 (Micromeritics) with a maximum pressure of 33,000 psi (228 MPa). After the mechanical tests, the specimens collected for the MIP tests had a volume of $\sim\!\!1$ cm 3 . After drying, the samples were put in a penetrometer with exactly 15 mL of volume—sample cup— and steam volume of 0.38 mL. The measurements were done in two steps. The first step used low pressure ranging from 0 to 50 psi (345 kPa), a resolution of 0.01 psi, and a pore diameter of 3.6–360 μm . The second step used high pressure up to 33,000 psi (228 MPa), with a resolution of 0.2 psi from 3000 psi to 33000 psi, and a pore diameter ranging from 6 to 0.005 μm . For each step, the transducer accuracy was $\pm 1\%$ of the full scale.

3. Results

3.1. XRD diffractograms and fourier transform infrared spectroscopy (FTIR) spectra

3.1.1. XRD diffractograms

The XRD patterns in Fig. 1 show the dominance of crystalline phases in the solid solution-based geopolymer composites. The XRD patterns of the raw materials are shown in Fig. 3 in the Supplementary materials: both MH and MK are amorphous whereas granite, pegmatite, and quartz are crystalline. The expression of the effectiveness of the geopolymerization is justified by the hump that is present in the diffraction pattern for all six formulations. Specimen Q, which showed a low extent of dissolution, had a significant expression of crystalline peaks of quartz. In turn, the samples with pegmatite had higher amorphous content based on the width of the hump, which varied from 25° to 35° in the 2θ range. The variation in the MH content between 15 and 25 wt% (R1 vs. R3) contributed to progressively reducing the expression of the hump due to the reduction in the overall amorphous gel content. The gel content is directly linked to the nature of the solid precursor (Nana et al., 2019). While specimen Q maintained almost all of the original peaks in the final geopolymer product, only the principal peaks were affected in the solid solution due to a larger extent of dissolution during geopolymerization compared to the quartz sand sample (Q).

3.1.2. FTIR spectra

Fig. 2 displays the FTIR spectra for all six formulations. Specimen Q showed principal bands centered at 1200 cm⁻¹, 1002 cm⁻¹, and 1064 cm⁻¹, which corresponded to the vibrating bands of crystalline quartz. The high values of the peaks were correlated with quartz sand's low ability to be dissolved, and these high values participated in the geopolymer network where more Q2 and Q3 species are visible, at approximately 849 cm⁻¹ (R1, R2, and R3). For R1, the principal characteristics of the aluminosilicates appeared at 994 cm⁻¹, which is in line with Tchakoute et al.'s (2017) finding for a good polymerized network of geopolymers. The peaks shifted to 991 cm⁻¹ for R2, R3, and D, confirming the relatively high volume of N-A-S-H+ polysialate geopolymer in those matrices (Fig. 2); here polysialate geopolymer refers to MKbased geopolymer. The volume fraction of quartz in the pegmatite could explain the relatively high value of 995 cm⁻¹ found for R1, R2, R3, and D. The carbonate peaks (anorthite, albite, and microcline) were relatively significant in samples with a high volume of reactive species N-A-S-H+ polysialate geopolymer — to the potential competition between N-A-S-H formation and carbonates. The relatively high volume

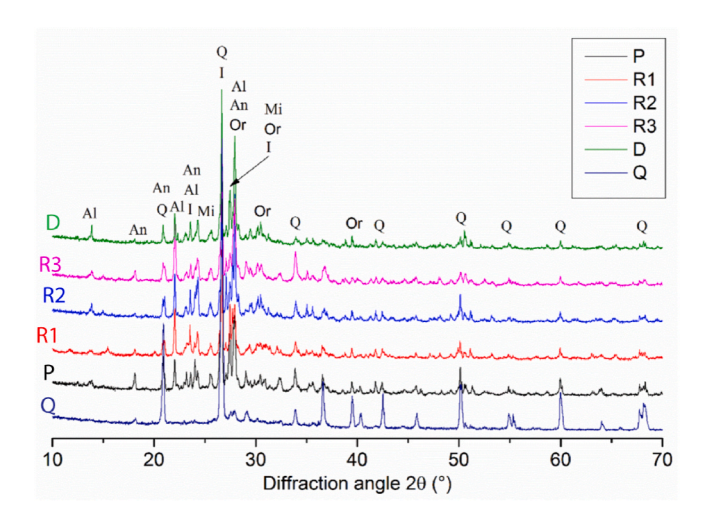


Fig. 1. XRD patterns of different compositions of IPCs. An: Anorthite; Al: Albite; I: Illite; Or: Orthose; Mi: Microcline; Q: Quartz.

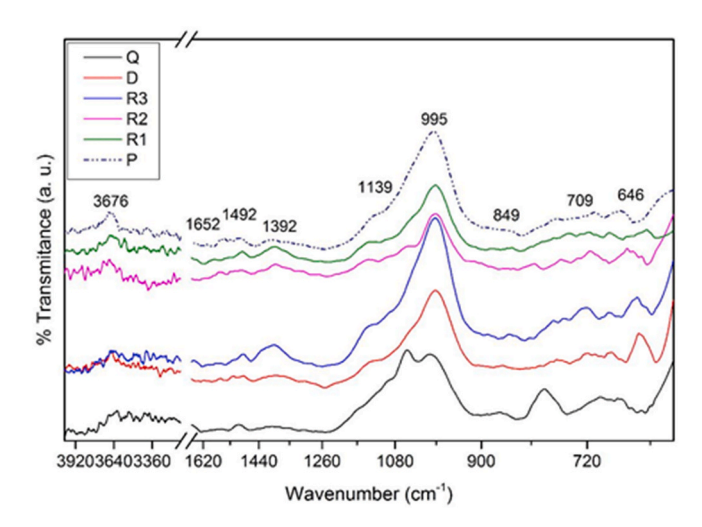


Fig. 2. FTIR patterns of different compositions of IPCs.

of quartz sand and low volume of N-A-S-H $\,+\,$ polysialate geopolymer allowed for more chemical stability.

3.2. SEM micrographs

Figs. 3–7 show the morphology of solid solution-based inorganic polymer composites of selected compositions using backscattered environmental electron scanning microscopy. At low magnification, $55\times$, (Fig. 3), each micrograph presents a dense and compact structure with the formation of few pores due to air bubbles. Independently upon the calcined clay used to increase the reactivity of fine powders, the resulting microstructures were homogeneous and dense.

At magnification $500\times$ and $1000\times$ (Figs. 4 and 6), a granular and microporous microstructure is observed. A reduction in the grain size is observed compared to the raw material initial size, which points to a partial dissolution of raw materials following geopolymerization. A digital image analysis of the back scattered scanning electron micrographs was conducted using the NIH-funded image analysis software ImageJ. Fig. 5 displays the grain size distribution for inorganic polymer composites. The dominant particle size is $18~\mu m$, $9~\mu m$, $10~\mu m$, $15~\mu m$, $27~\mu m$, and $9~\mu m$ respectively for Q, P, R1, R2, R3, and D. In particular, for all inorganic polymer composites, the dominant grain size is much less than the initial size of the raw materials, $63~\mu m$. This reduction in the grain size is evidence of the partial dissolution of raw materials following geopolymerization.

The morphology of the matrices at magnification $1000\times$ (Fig. 6) illustrates a decrease in the level of connectivity, particularly in the Q sample, due to the reduction in the reactive phases. The gel formed on the granite-based inorganic polymer composite (P) had matrices with more porous and broader reactive phases (Fig. 6) compared to the gel formed on the sand (Q). This can be explained by the fact that the quartz sand leaches primarily Si-based secondary minerals, while granite and pegmatite provide sufficient Al and Si-based secondary minerals for the high compactness of the matrices. Comparing the micrographs of pegmatite-based specimens at 85 wt% of fine particles added to 15 wt% of calcined clay (R3 vs. D), MH (R3 in Fig. 6f) showed excellent densification in comparison to MK (D in Fig. 6c). This densification was more regular and resulted in less porosity compared to MH.

At magnification $10,000 \times$, a strong bond was observed at the matrix-grain interface for most inorganic polymer composites: in Fig. 7, it is not possible to distinguish these partly dissolved particles from those involved in polymerization. The gel develops successfully to cover the surfaces of the grains and fill all the pores and voids, forming a compact microstructure. However, some micro-fissures were observed in the sand-based geopolymer composite (Q in Fig. 7 a), which are in line with

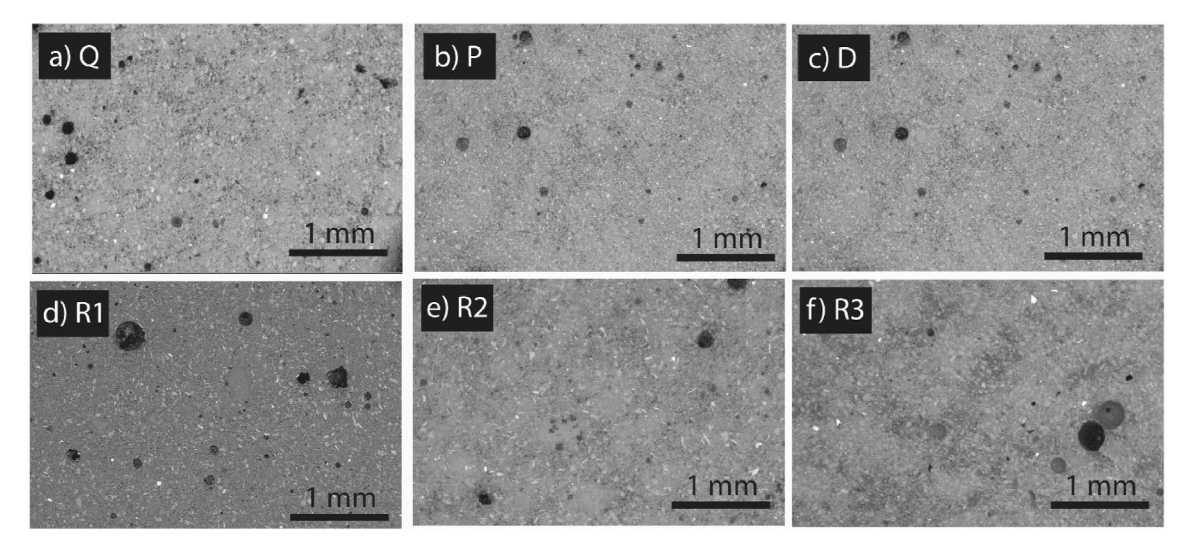


Fig. 3. ESEM micrographs of inorganic composites at magnification 55×.

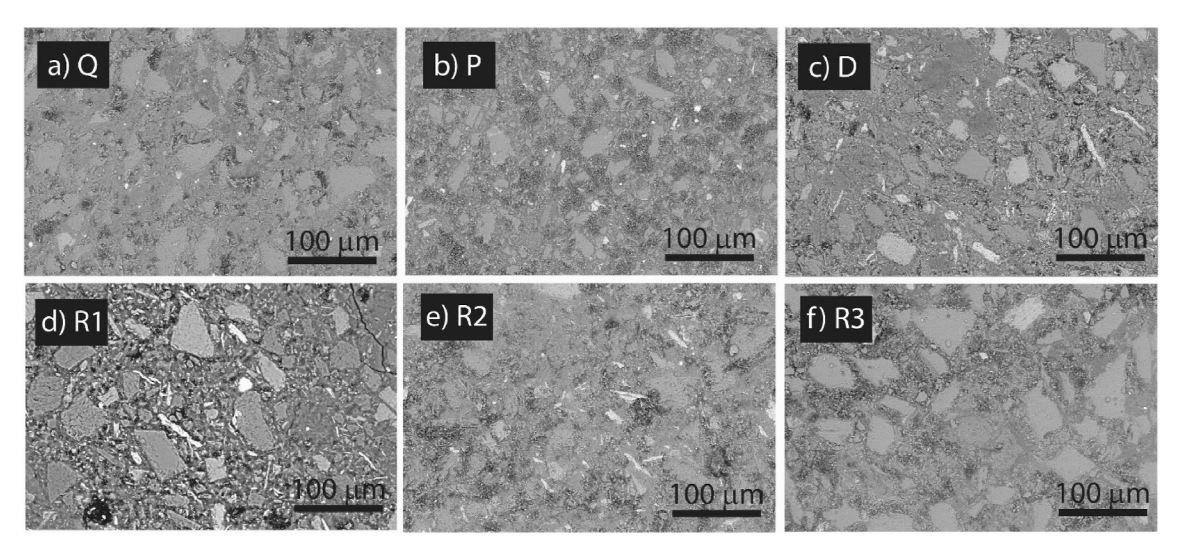


Fig. 4. ESEM micrographs of inorganic composites at magnification $500 \times$.

the level of dissolution and formation of both N-A-S-H and of polysialate geopolymer. The difficulties forming adequate polysialate geopolymer and N-A-S-H phases modify the interface behavior between the binder phase and reactive particles. The accumulation of more crystalline particles in the geopolymer gels created a stress gradient and induced micro-cracking compared to the feldspathic solid solutions (granite and pegmatite), in which the particles were maintained by the reactions occurring at the interphases of the particles. Nevertheless, overall the particles were strongly bonded to the matrix for most inorganic polymer composites. The partial dissolution of solid solution particles affected the particles surfaces' chemistry, and the semi- or incongruently dissolved particles remained intimately sealed to the chains of aluminosilicates that formed in the final matrix.

3.3. Pore size distribution

Figs. 8 and 9 display the results of the MIP testing. The cumulative pore volume of the solid solution-based geopolymer composites was approximately 18.75 mm 3 /g for the Q specimen. This specimen showed a principal pores band in the interval between 0.016 and 0.077 μ m. While it had a similar MH/solid solution ratio, specimen R2 had a relatively low cumulative pore volume of 16.12 mm 3 /g. The type of pore varied significantly depending on the amount of solid solution. MK and

MH favored both nanopores (less than 100 nm in size) and micropores (less than 10 μm in size). Meanwhile, for feldspathic solid solutions particles, nanopores were reduced and the development of a new class of porosity occurred, which was a little coarser and >1 mm in size, see Fig. 3. This process can be described as intergranular porosity forming from geopolymer gel and solid solutions particles. Comparing the specimens obtained from MH with those from MK (D), we noted that the geopolymer composites based on MH presented a lower cumulative pore volume (14.18 mm $^3/g$) than those from MK (18.77 mm $^3/g$) at the same composition (85 wt% of feldspathic solid solution and 15 wt% of calcined clay). A similar trend was observed with the pore size distribution: the pore band was around 0.012–0.095 μm for MH-based geopolymer composites and 0.021–0.120 μm for MK-based geopolymer composites.

3.4. Mechanical properties

The flexural strength of the geopolymer composites varied from 26.31 MPa for specimen Q to 36.42 MPa for formulation P (Fig. 10). Specimens P, R2, R3, and D had high values of flexural strength, which explains the high performance of their solid solutions-based geopolymer composites. The high value of the flexural strength can be explained by the reduced cumulative pore volume: 16 mm³/g for R2 and 14 mm³/g

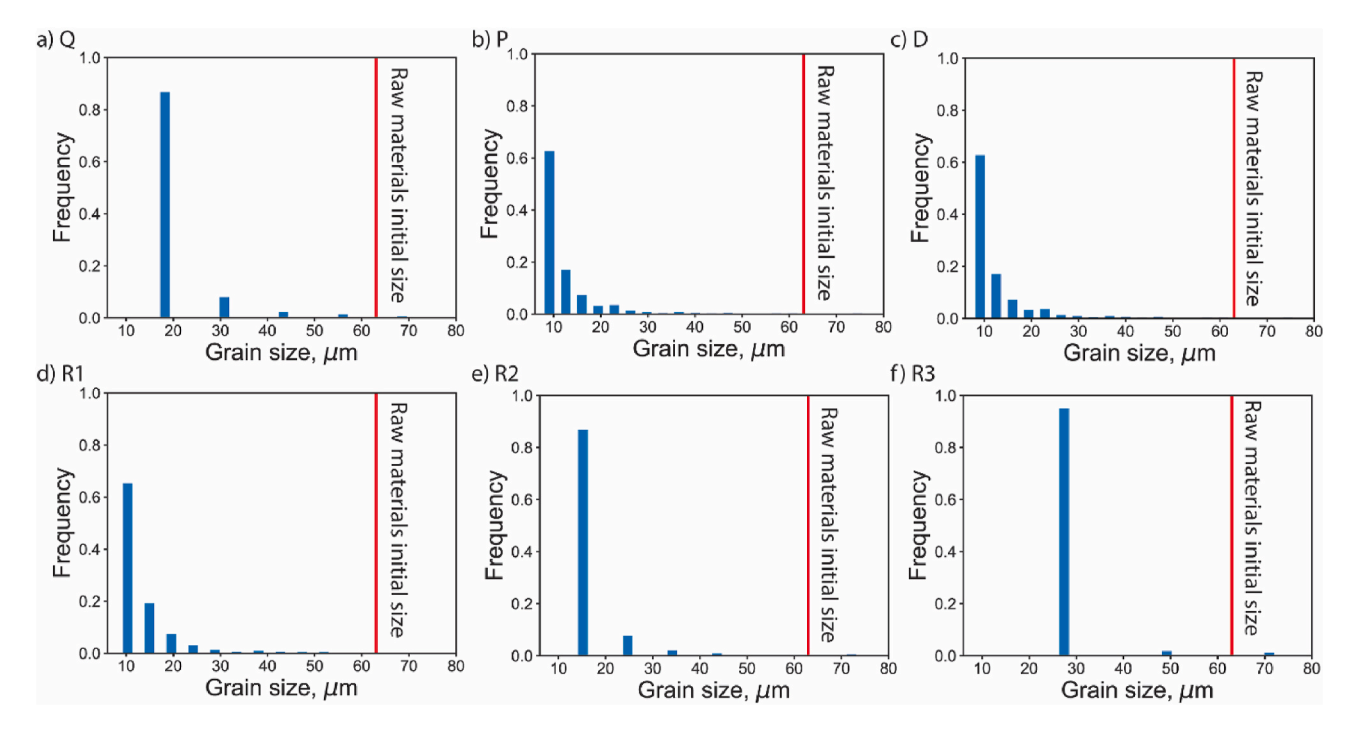


Fig. 5. Particle size distribution of hardened inorganic polymer composites.

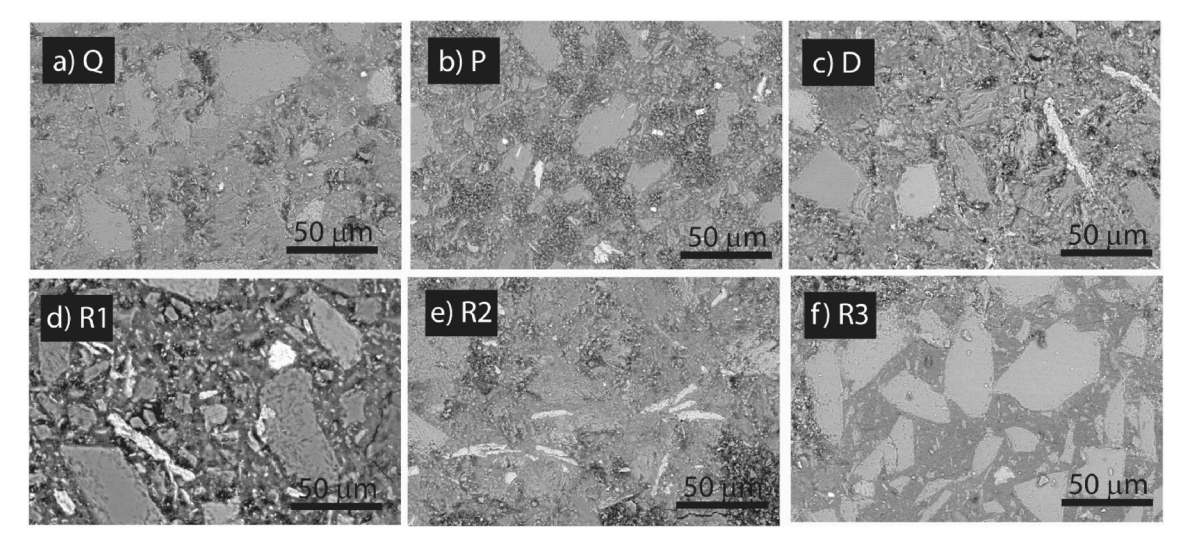


Fig. 6. ESEM micrographs of inorganic composites at magnification 1000 \times .

for R3 (Fig. 8). Even though the cumulative pore volume (18.78 mm^3/g) was relatively higher for specimen P compared to specimens R1 and D, only specimen P exhibited a high fraction of fine pores. The compressive strength followed the trend of the flexural strength, with Q and R1 having the lowest strengths at 96.50 and 96.84 MPa, respectively (Fig. 11). However, the values of the compressive strength in the R and D series were not very different from that of Q (100 MPa).

The fracture toughness for the geopolymer composites is displayed in Fig. 12. The fracture toughness ranged from 0.49 MPa \sqrt{m} (R3) to 0.60 MPa \sqrt{m} (Q). In general, the stronger the geopolymer composite, the more brittle it was and the lower the fracture toughness it had. In particular, the geopolymer composites with the highest fraction of fine particles also exhibited the lowest values for fracture toughness. Fig. 13 shows the fracture micro-mechanisms of geopolymer composites: micro-cracking, debris formation, intragranular fracture, and ligament bridging. The most prevalent fracture micro-mechanisms were

microcracking and intragranular fracture. These were due to the fact that both the particles and the matrix were brittle and because of the perfect bonding at the particle/matrix interface. As a result, when selecting a mix design for geopolymer composites, a trade-off must be found between strength and fracture toughness. The composite R2 presented the ideal trade-off between high strength and high fracture toughness.

3.5. Micromechanical analysis

The micromechanical analysis of inorganic polymer cements considered in this study is shown in Figs. 14 and 15. The indentation data are shown in the (M,H) space in Fig. 14, along with the specific clusters identified. The volume fraction of the different microconstituents is plotted in Fig. 15. Table 3 lists the characteristics of each phase for all six formulations of inorganic polymer composites. Based on

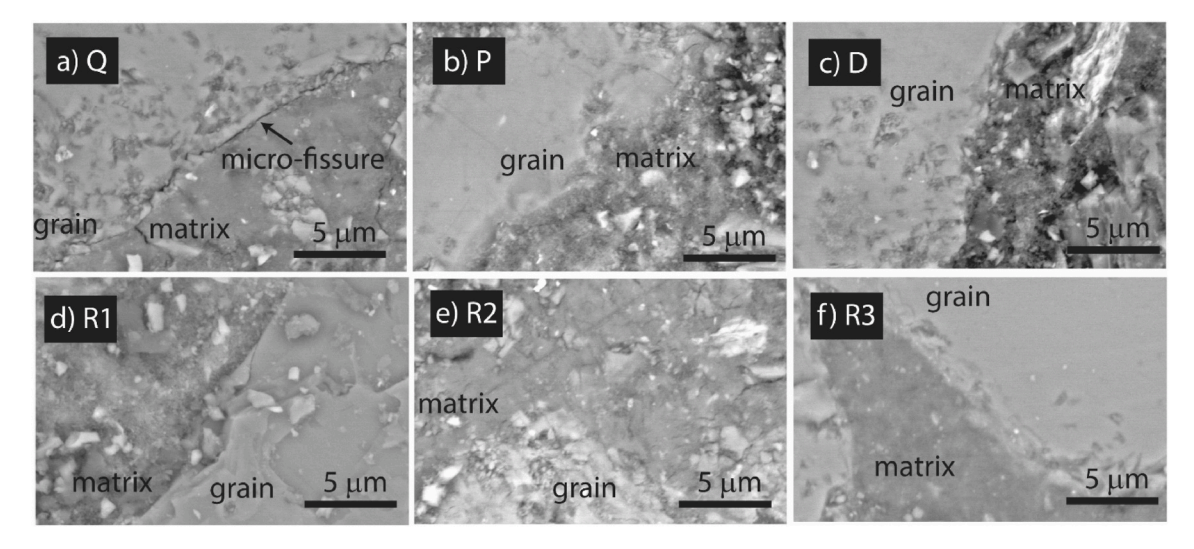
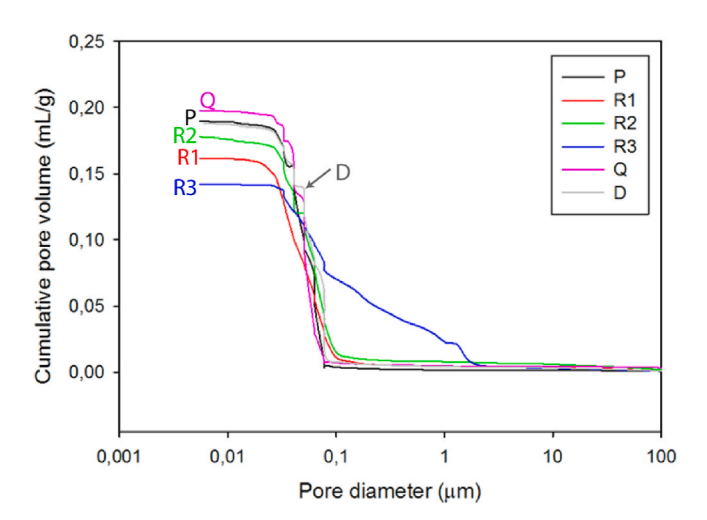


Fig. 7. ESEM micrographs of the grain/matrix interface for inorganic composites at magnification $10,000 \times ...$



 $\begin{tabular}{ll} Fig.~8. Cumulative~pore~volume~versus~pore~diameter~for~different~compositions~of~IPCs. \end{tabular}$

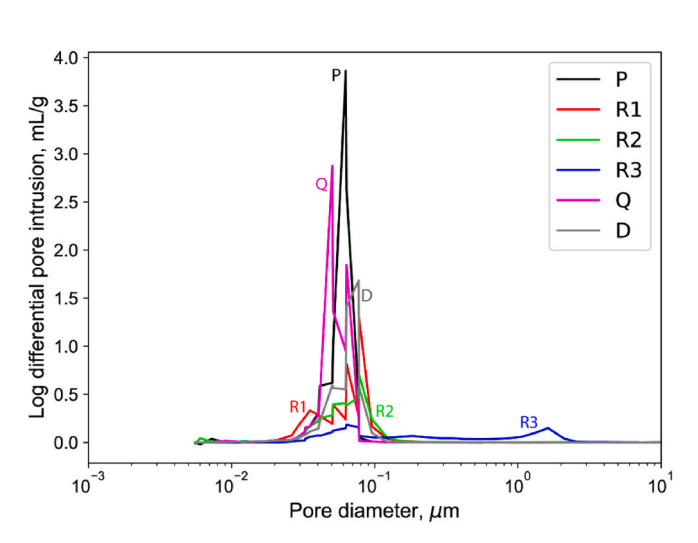


Fig. 9. Pore size distribution of the different formulations of solid solutions-based geopolymer composites.

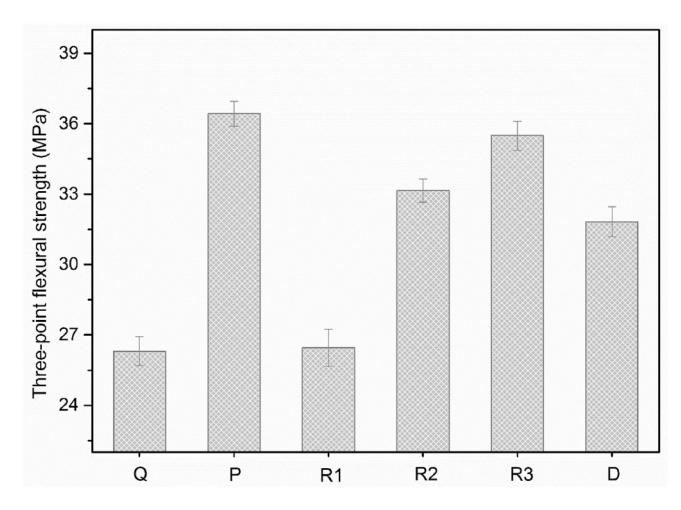


Fig. 10. Variations in the three-point flexural strength of geopolymer composites.

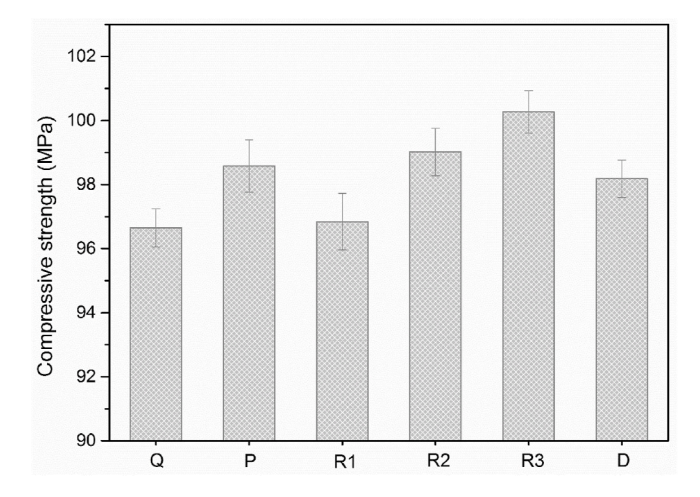


Fig. 11. Variations in the compressive strength of different compositions of geopolymer composites.

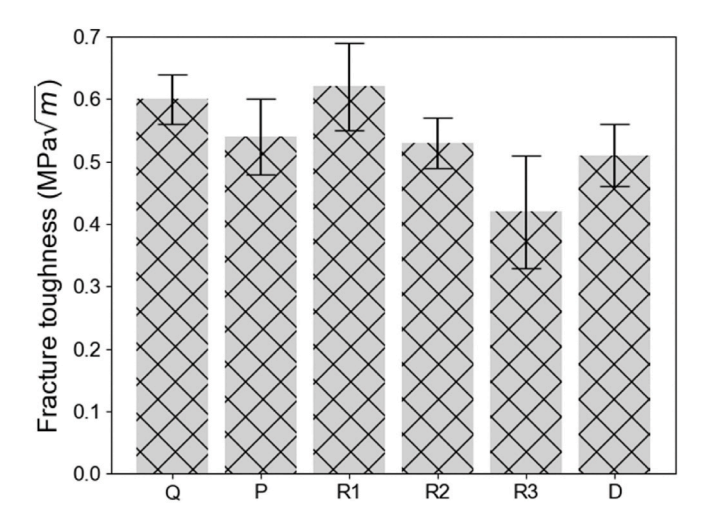


Fig. 12. Fracture toughness values for IPCs.

the mechanical signature, we distinguished four types of micro-constituents: polysialate geopolymer—which is the MK gel, N-A-S-H, feldspathic rock particles, and C-A-H phases. For all inorganic polymers except the R3 system, polysialate geopolymer was the dominant phase, with a volume fraction of 41–55%. The highest value of the indentation modulus *M* of the polysialate geopolymer occurred for pegmatite with an MH-based geopolymer (R1, R2, and R3 systems), which yielded values of 12.53–12.82 GPa. The lowest value was obtained for quartz with an MH-based geopolymer at 6.78 GPa. For granite with MH and for pegmatite with an MK-based geopolymer, the indentation modulus of the amorphous matrix was 9.32 GPa and 9.47 GPa, respectively. The variations in indentation modulus can be attributed to changes in the chemistry of the polysialate geopolymer. For instance, the Si/Al ratio is

known to strongly influence the elastic modulus of polysialate geopolymers [36].

The indentation modulus values for the polysialate geopolymer phase, 6.78–12.82 GPa, agree with elastic modulus values reported for pure amorphous metakaolin-based geopolymer [37,38]. Moreover, we identified the N-A-S-H gel for the solid solution inorganic polymer systems studied (Fig. 13). The N-A-S-H gel forms as the residual solution reacts with the aluminate and silicate groups within the fine particles. The N-A-S-H gel can be identified based on its mechanical signature: the indentation modulus was in the range of 20.70–31.76 GPa. These values agree with reported values of the indentation modulus for the N-A-S-H gel after 28 days of curing [39,40]. For all inorganic systems except R3, the N-A-S-H gel phase accounted for 15–24% of the total volume.

We noted the presence of residual feldspathic rock particles, which point to a partial dissolution of the fine particles. The highest dissolution rates were obtained for the P and R1 systems. Meanwhile, the lowest fine particle dissolution rates were obtained for the R3 and D systems, which were characterized by a low fraction of MH and MK, respectively. Finally, we observed the precipitation of C-A-H phases. The C-A-H phases were characterized by high values of the indentation modulus (>100 GPa). C-A-H formation was observed at low mass fractions of MK and MH (<15% and <20%, respectively).

4. Discussion

4.1. Solid solution reactivity and inorganic polymer phase evolution

4.1.1. Reactivity of the feldspar solid solutions

Similar to solutions with MK, the reaction of feldspathic powders (as a principal precursor) was altered by the presence of MH. As evidence, the broad halo in XRD patterns (between 20° and 35° in the $2~\theta$ range) corresponded to the three-dimensional structure in the geopolymer network. Fewer particles participated in the geopolymerization process

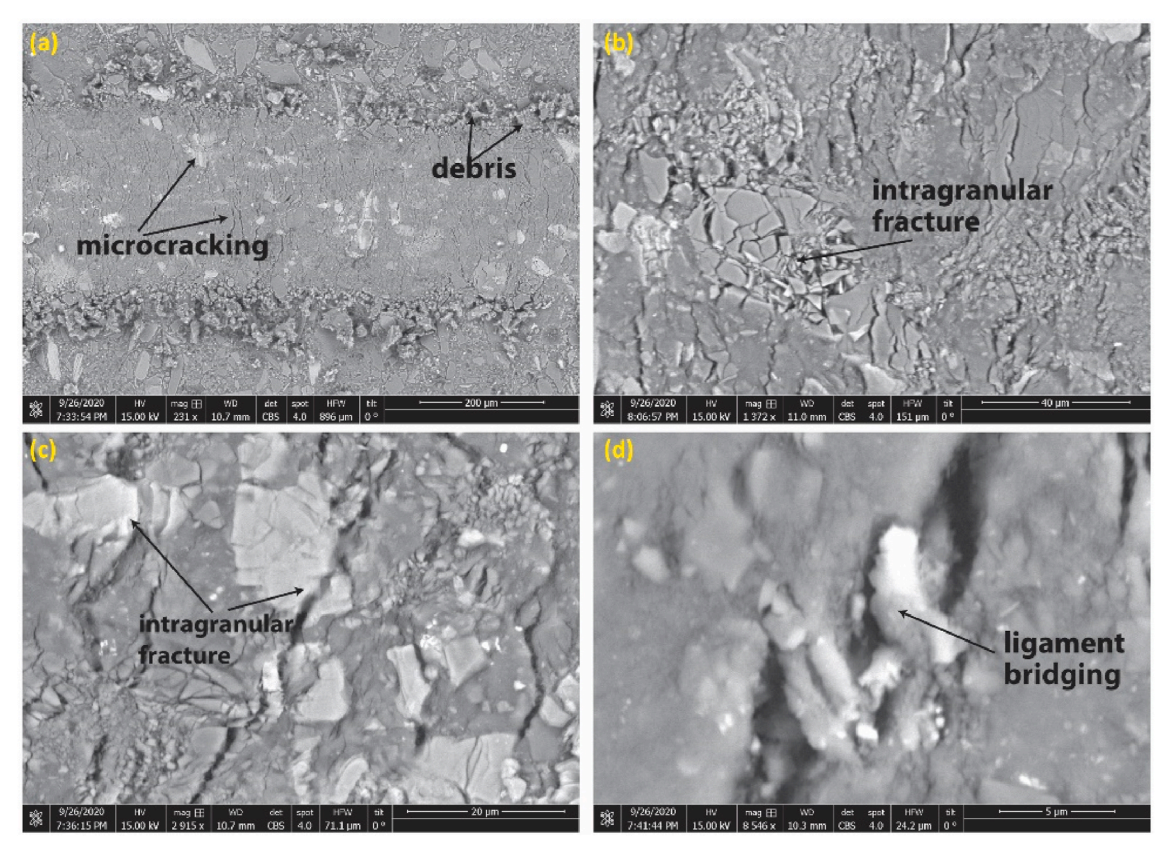


Fig. 13. Fracture micro-mechanisms for IPCs.

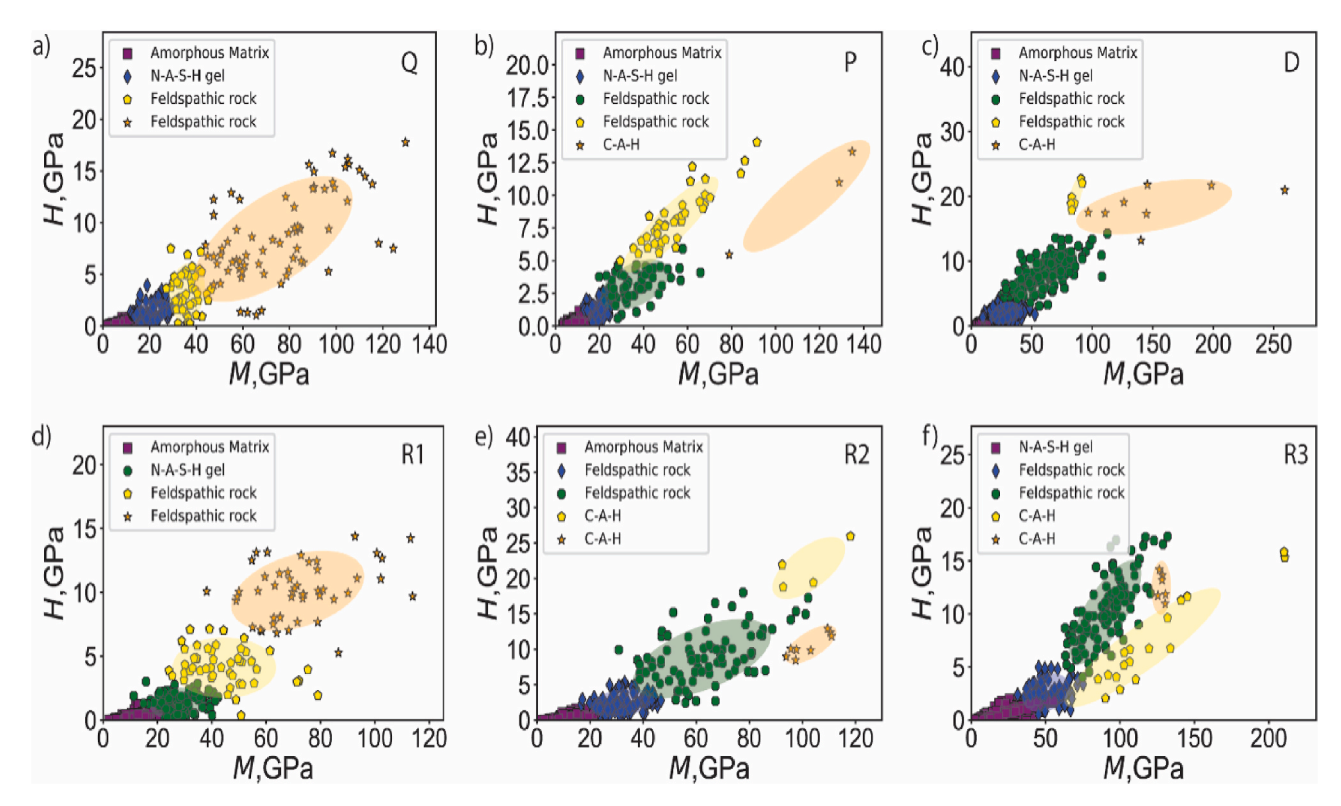


Fig. 14. (a) Statistical deconvolution of grid nanoindentation tests on IPCs. Each data point represents a single indentation test. For R1 and R2 specimens, 400 tests were conducted per specimen. For all remaining specimens, 441 indentation tests were conducted per specimen. *M* is the indentation modulus in GPa, and *H* is the indentation hardness in MPa. (b) Variation of the fracture toughness of different compositions of geopolymer composites. (c) Fracture micro-mechanisms of geopolymer composites.

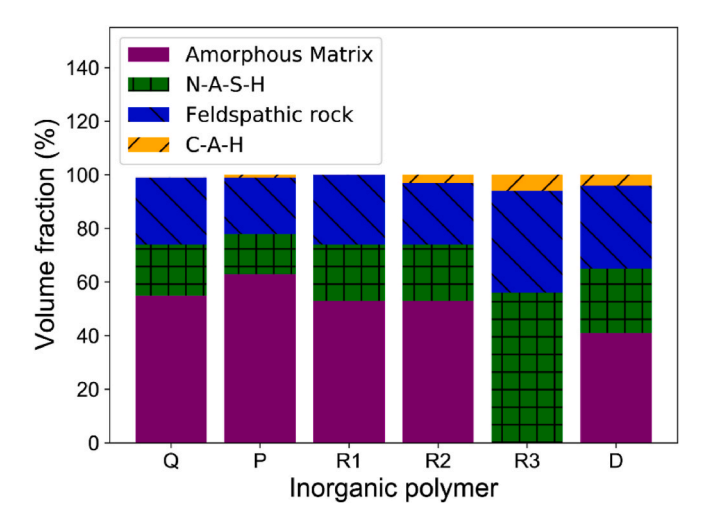


Fig. 15. Phase distribution of IPCs. The volume fraction is shown for each micro-constituent: amorphous matrix, N-A-S-H gel, feldspathic rock particles, and C-A-H.

due to their crystallinity, as illustrated by the decreased number and uncharged nature of the peaks observed on the XRD patterns of inorganic polymer composites compared to those observed on the solid precursors (granite, quartz sand, and pegmatite) [26] The most abundant of these peaks were for anorthite, albite, and quartz. The major peaks observed after the geopolymerization reaction were for illite, orthose, microcline, and albite. The specimens based on quartz sand (Q) presented higher crystallinity compared to those based on granite (P) and pegmatite (R1 or D). For samples with high crystallinity, the high intensity of the quartz peaks remained almost unchanged. When the

Table 3 Mechanical phases of IPCs. μ_M (respectively σ_M) is the mean value (respectively standard deviation) of the indentation modulus in GPa. μ_H (respectively σ_H) is the mean value (respectively standard deviation) of the indentation hardness in MPa. Vol is the volume fraction in percent. 400–441 indentations were conducted for each inorganic polymer composite.

IPC	Phase	(μ_{M}, σ_{M}) (GPa)	(μ_H, σ_H) (GPa)	Vol (%)
Q	Amorphous Matrix	(6.78,3.39)	(0.21, 0.27)	55
	N-A-S-H gel	(20.70,5.25)	(1.28, 0.91)	19
	Feldspathic rock	(36.00, 5.19)	(3.28, 1.88)	9
	Feldspathic rock	(73.08,2.38)	(8.41,4.22)	16
P	Amorphous Matrix	(9.32,3.34)	(0.33, 0.29)	63
	N-A-S-H gel	(19.34, 3.02)	(1.10, 0.69)	15
	Feldspathic rock	(36.02,10.64)	(3.15, 1.31)	12
	Feldspathic rock	(52.49,14.90)	(7.77, 2.51)	9
	C-A-H	(114.08,20.06)	(9.94,2.96)	1
R1	Amorphous Matrix	(12.53, 4.93)	(0.32, 0.35)	53
	N-A-S-H gel	(27.37,6.90)	(1.28, 0.80)	21
	Feldspathic rock	(44.53,1.32)	(4.11,1.60)	14
	Feldspathic rock	(71.61,1.70)	(10.12, 2.15)	12
R2	Amorphous Matrix	(12.82,5.31)	(0.51, 0.42)	53
	N-A-S-H gel	31.76 ± 7.94	2.43 ± 1.29	21
	Feldspathic rock	62.13 ± 18.02	8.69 ± 3.83	23
	C-A-H	102.45 ± 9.41	21.48 ± 2.97	1
	C-A-H	103.13 ± 6.52	10.68 ± 1.79	2
R3	N-A-S-H gel	25.64 ± 14.15	0.85 ± 0.64	56
	Feldspathic rock	(50.17,10.93)	(2.58, 1.19)	13
	Feldspathic rock	(90.07,16.73)	(10.16, 3.38)	25
	C-A-H	(115.23,36.73)	(6.83, 3.89)	5
	C-A-H	(127.67,4.11)	(12.47, 1.71)	1
D	Amorphous Matrix	(9.54,3.83)	(0.30, 0.31)	42
	N-A-S-H gel	(28.51,9.07)	(1.99, 1.09)	23
	Feldspathic rock	(60.00, 18.88)	(8.06,2.70)	32
	Feldspathic rock	(85.96, 3.91)	(20.00, 1.98)	2
	C-A-H	(151.16,44.92)	(18.37,2.88)	2

same quantity of solid solution of pegmatite was used with different calcined clays (R3 and D), similar curved XRD patterns were observed. This can be explained by the fact that the reaction of feldspathic powders in an alkaline solution depends mostly on its amorphous/crystalline fraction. The variation in the quantity of ground particles, which ranged from 75 wt% (R1) to 85 wt% (R3), was correlated with the broad peak characteristic of the disordered structure of pegmatite-based IPC composites, which decreased in intensity and shifted slightly towards a lower 2 θ range, indicating the effectiveness of the increase in reactivity with MH.

4.1.2. Phase evolution for IPCs

Regarding the phase distribution in the solid solutions matrices, Table 3 shows that pegmatite-based geopolymer composites were present in ~65 vol% of the phases associated with N-A-S-H and polysialate geopolymer when using either MK or MH at a mass fraction of 15 wt%. When the MH content was increased to 20 or 25 wt%, the N-A-S-H + polysialate geopolymer increased to >70 vol%. Finally, the N-A-S-H + polysialate geopolymer increased to 74% for quartz MH and 78% for granite MH. The heterogeneity of the phases found in granite and the relative fineness of their particles could explain the high volume of the N-A-S-H amorphous gel achieved with specimens of formulation P with 15 wt% of MH. These results show the degree of geopolymerization required to ensure high-strength solid solutions-based geopolymer composites. After 12 months of curing, the geopolymer composites showed a complex matrix with phases closely interlocked with one another for optimal densification, see Fig. 6.

The solid solutions developed Al-rich phases in the nature of C-A-H, which contributed significantly to the strengthening mechanism although to a relatively low extent. Al-rich oligomers in cementitious phases are known to impart mechanical strength. When the amount of MK was $>\!25$ wt%, the C-A-H phases were difficult to identify in the matrix. This could be due to the differential dissolution of the solid precursor during geopolymerization. When the volume of MH was high, the dissolution of the solid precursor was modified in terms of the kinetic availability of Al, Si, and Ca. Based on this result, it seems that the strength of a dissolved solid precursor is greater when the soluble species come from the solid solution.

4.2. Strengthening mechanisms

The strengthening mechanisms included amorphous matrix strengthening in relation to the partial dissolution of feldspar particles as well as the formation of the N-A-S-H gel. The values of the flexural strength and compressive strength were linked to the fraction of N-A-S-H and amorphous content developed during geopolymerization. The partial dissolution of feldspar solid precursors limited the formation of N-A-S-H phases; in turn, larger fractions of amorphous and N-A-S-H phases affected the strength. Moreover, when N-A-S-H formed, the existence of a large volume of soluble silica increased the densification of the matrix, strengthening the gel bonds, and reducing the porosity. However, in this study, the incongruent dissolution of solid solution feldspar particles contributed to improving the bond quality because the remaining incongruent dissolved grains were embedded in the gel and homogeneously dispersed throughout the matrix.

The reduction of the porosity was an additional strengthening mechanism. In the R2 and R3 series, the capillary porosity (band between 0.1 and 1 μm for R2 and >1 μm for R3) was linked to a larger volume of N-A-S-H and amorphous phase developed in relation with the viscosity of the paste. The filler's effect in the P series was due to the small particles of residual powders. Furthermore, the interfacial bond at the gel particle surface also acted as a strengthening mechanism, justifying the variation of the mechanical strength of the solid solution-based geopolymer composites.

5. Conclusions

The scientific objectives of this work were to monitor the role of the limited extent of the dissolution of solid solutions (feldspathic particles) in the development of high-strength chemical bonds and the reduction in pore size in high-performance geopolymer composites. The results of statistical nanoindentation, scratch testing, MIP, and macroscopic mechanical testing led to the following conclusions:

- Using statistical nanoindentation, we identify two distinct amorphous phases: polysialate geopolymer and N-A-S-H. The polysialate geopolymer phase has an indentation modulus of 6–12 GPa, value that agrees with reported indentation modulus values for amorphous metakaolin geopolymer. In addition, the N-A-S-H phase has an indentation modulus of 19.34–31.76–29 GPa and is very distinct from the polysialate geopolymer phase.
- Geopolymer composites with high mechanical performance can be achieved by reducing the expression of the N-A-S-H + polysialate geopolymer binder in the context of the incongruent dissolution of fine powders.
- A particularly high strength was observed as a result of the N-A-S-H
 + polysialate geopolymer/particles ratio. When used in a sufficient
 amount to cover the partially dissolved particles, the N-A-S-H +
 polysialate geopolymer gel established strong bonds while
 decreasing capillary porosity.
- The correlation between the nature of the solid solution and the
 extent of dissolution made it possible to design an appropriate prediction mechanism regarding the effective role of the reactive phase
 and the efficiency of the interparticle interaction in the development
 of high-strength geopolymer composites.
- The use of solid solutions in fine powders represents an important part of industrial solid waste reduction. N-A-S-H + polysialate geopolymer content presents a solid solution-based geopolymer composites for the future development of environmentally friendly and sustainable composites.
- The high mechanical performance and low porosity achieved make solid solutions-based geopolymer composites a promising candidate for structural engineering applications and the reproduction of natural stones.

Declaration of competing interest

The authors declare that they have no known competing financial interests or personal relationships that could have appeared to influence the work reported in this paper.

Acknowledgments

This work was supported by the Royal Society (Global Challenge Research Fund) and the African Academy of Science through the FLAIR Fellowship (No: FLR/2014402) presented to Dr. Elie Kamseu. This work was also supported by the National Science Foundation (Grant No. CMMI 1829101 presented to Dr. Ange-Therese Akono).

Appendix A. Supplementary data

Supplementary data to this article can be found online at https://doi.org/10.1016/j.cemconcomp.2021.104241.

References

- Y. Zhang, P. He, J. Yuan, C. Yang, D. Jia, Y. Zhou, Effects of graphite on the mechanical and microwave absorption properties of geopolymer based composites, Ceram. Int. 43 (2016) 2325–2332.
- [2] Q. Wan, F. Rao, S. Song, D.F. Cholico-Gonzalez, N.L. Ortiz, Combination formation in the reinforcement of metakaolin geopolymers with quartz sand, Cement Concr. Compos. 80 (2017) 115–122.

- [3] T. Korim Balczár, A. Dobrádi, Correlation of strength to apparent porosity of geopolymers – understanding through variations of setting time, Construct. Build. Mater. 93 (2015) 983–988.
- [4] H.A. Abdel-Gawwad, K.A. Khalil, Application of thermal treatment on cement kiln dust and feldspar to create one-part geopolymer cement, Construct. Build. Mater. 187 (2018) 231–237.
- [5] H. Tan, X. Deng, X. He, J. Zhanga, X. Zhanga, Y. Su, Y. Yang, Compressive strength and hydration process of wet-grinded granulated blast-furnace slag activated by sodium sulfate and sodium carbonate, Cement Concr. Compos. 97 (2019) 387–398.
- [6] V.F. Barbosa, K.J. MacKenzie, Thermal behaviour of inorganic geopolymers and composites derived from sodium polysialate, Mater. Res. Bull. 38 (2003) 319–331.
- [7] S.A. Bernal, J. Bejarano, C. Garzón, R.M. de Gutiérrez, S. Delvasto, E.D. Rodríguez, Performance of refractory aluminosilicate particle/fiber-reinforced geopolymer composites, Compos. B Eng. 43 (2012) 1919–1928.
- [8] T. Bakharev, Resistance of geopolymer materials to acid attack, Cement Concr. Res. 35 (2005) 658–670.
- [9] J. Davidovits, Geopolymer: ceramic-like inorganic polymers, J. Ceram. Sci. Technol. 350 (2017) 335–350.
- [10] D.C. Pereira, G. Amaral-Labat, G.F.B. Lenz e Silca, Effect of sawdust as porosity agent on final properties of geopolymers, Ceramica 65 (2019) 104–109.
- [11] C. Shi, B. Qu, J.L. Provis, Recent progress in low-carbon binders, Cement Concr. Res. 122 (2019) 227–250.
- [12] S.K. Nath, S. Kumar, Role of particle fineness on engineering properties and microstructure of fly ash derived geopolymer, Construct. Build. Mater. 233 (2020), 117304.
- [13] E. Kamseu, M. Cannio, E.A. Obonyo, F. Tobias, M.C. Bignozzi, V.M. Sglavo, C. Leonelli, Metakaolin-based inorganic polymer composite: effects of fine aggregate composition and structure on porosity evolution, microstructure and mechanical properties, Cement Concr. Compos. 53 (2014) 258–269.
- [14] C.R. Kaze, P. Venyite, A. Nana, N.J. Deutou, H.K. Tchakoute, H. Rahier, E. Kamseu, U.C. Melo, C. Leonelli, Meta-halloysite to improve compactness in iron-rich laterite-based alkali activated materials, Mater. Chem. Phys. 239 (2020), 122268.
- [15] N. Ali, O. Canpolat, Y. Aygormez, M.M. Al-Mashhadani, Evaluation of the 12–24 mm basalt fibers and boron waste on reinforced metakaolin-based geopolymer, Construct. Build. Mater. 251 (2020), 118976.
- [16] H.K. Tchakoute, C.H. Ruscher, J.N.Y. Djobo, B.B.D. Kenne, D. Njopwouo, Influence of gibbsite and quartz in kaolin on the properties of metakaolin-based geopolymer cements, Appl. Clay Sci. 107 (2015) 188–194.
- [17] H.K. Tchakoute, C.H. Rüscher, E. Kamseu, J.N.Y. Djobo, C. Leonelli, The influence of gibbsite in kaolin and the formation of berlinite on the properties of metakaolinphosphate-based geopolymer cements, Mater. Chem. Phys. 199 (2017) 280–288.
- [18] E. Kamseu, H. Mohamed, J.C. Sofack, D. Chaysuwan, H.K. Tchakoute, J.N. Y. Djobo, S. Rossignol, C. Leonelli, Moisture control capacity of geopolymer composites: correlation of the bulk composition—pore network with the absorption—desorption behavior, Transport Porous Media 122 (2018) 77–95.
- [19] R.C. Kaze, L.M. Beleuk à Moungam, M. Cannio, R. Rosa, E. Kamseu, U.C. Melo, C. Leonelli, Microstructure and engineering properties of Fe₂O₃(FeO)-Al₂O₃-SiO₂ based geopolymer composites, J. Clean. Prod. 199 (2018) 849–859.
- [20] H. Xu, J.S.J. van Deventer, Factors affecting the geopolymerization of alkalifeldspars, Miner. Metall. Process. 19 (2002) 209–214.
- [21] H. Xu, J.S.J. van Deventer, The effect of alkali metals on the formation of geopolymeric gels from alkali-feldspars, Colloid. Surface. Physicochem. Eng. Aspect. 216 (2003) 27–44.

- [22] D. Gonzalez-Garcia, L. Tellez-Jurado, J.F. Jiménez-Alvarez, H. Balmori-Ramirez, Structural study of geopolymers obtained from alkali-activated natural pozzolan feldspars, Ceram. Int. 43 (2016) 2606–2613.
- [23] G. Habert, J.B. d'Espinose de Lacaillerie, N. Roussel, An environmental evaluation of geopolymer based concrete production: reviewing current research trends, J. Clean. Prod. 19 (2011) 1229–1238.
- [24] C.E. White, J.L. Provis, A. Llobet, T. Proffen, J.S.J. van Deventer, Evolution of local structure in geopolymer gels: an in situ neutron pair distribution function analysis, J. Am. Ceram. Soc. 94 (2015) 3532–3539.
- [25] E. Kamseu, C. Djangang, P. Veronesi, A. Fernanda, U.C. Melo, V.M. Sglavo, C. Leonelli, Influence of fine aggregates on the microstructure, porosity and chemico-mechanical stability of inorganic polymer concretes, Construct. Build. Mater. 96 (2015) 473–483.
- [26] J. Ngouné Nana, R.C. Kaze, L. Boubakar, S.K. Tchounang, H.K. Tchakouté, E. Kamseu, C. Leonelli, Room-temperature alkaline activation of feldspathic solid solutions: development of high strength geopolymers, Construct. Build. Mater. 195 (2019) 258–268.
- [27] A.T. Akono, P.M. Reis, F.J. Ulm, Scratching as a fracture process: from butter to steel, Phys. Rev. Lett. 106 (2011) 204302.
- [28] A.T. Akono, N.X. Randall, F.J. Ulm, Experimental determination of the fracture toughness via microscratch tests: application to polymers, ceramics, and metals, J. Mater. Res. 27 (2012) 485–493.
- [29] A.T. Akono, F.J. Ulm, Fracture scaling relations for scratch tests of axisymmetric shape, J. Mech. Phys. Solid. 60 (2012) 379–390.
- [30] A.T. Akono, F.J. Ulm, An improved technique for characterizing the fracture toughness via scratch test experiments, Wear 313 (2014) 117–124.
- [31] W.C. Oliver, G.M. Pharr, An improved technique for determining hardness and elastic modulus using load and displacement sensing indentation experiments, J. Mater. Res. 7 (1992) 1564–1583.
- [32] W.C. Oliver, G.M. Pharr, Measurement of hardness and elastic modulus by instrumented indentation: advances in understanding and refinements to methodology, J. Mater. Res. 19 (2004) 3–20.
- [33] G. Constantinides, F.J. Ulm, The effect of two types of CSH on the elasticity of cement-based materials: results from nanoindentation and micromechanical modeling, Cement Concr. Res. 34 (2004) 67–80.
- [34] L. Sorelli, G. Constantinides, F.J. Ulm, F. Toutlemonde, The nano-mechanical signature of ultra high performance concrete by statistical nanoindentation techniques, Cement Concr. Res. 38 (2008) 1447–1456.
- [35] G. Cowan, Statistical Data Analysis, 1998. Oxford.
- [36] P. Duxson, G.C. Lukey, J.S. Van De Venter, S.W. Mallicoat, W.M. Kriven, Microstructural characterisation of metakaolin-based geopolymers, Ceram. Trans. 165 (2005) 71–85.
- [37] R.A.S. Ribeiro, M.S. Ribeiro, W.M. Kriven, A review of particle-and fiber-reinforced metakaolin-based geopolymer composites, J. Ceram. Sci. Technol. 8 (2017) 307–322.
- [38] A.T. Akono, Fracture behavior of metakaolin-based geopolymer reinforced with carbon nanofibers, Int. J. Ceram. Eng. Sci. 2 (2020) 234–242.
- [39] J. Němeček, V. Šmilauer, L. Kopecký, Nanoindentation characteristics of alkaliactivated aluminosilicate materials, Cement Concr. Compos. 33 (2011) 163–170.
- [40] V. Šmilauer, P. Hlaváček, F. Škvára, R. Šulc, L. Kopecký, J. Němeček, Micromechanical multiscale model for alkali activation of fly ash and metakaolin, J. Mater. Sci. 46 (2011) 6545–6555.